

Geometrodynamics: The Nonlinear Dynamics of Curved Spacetime

Mark A. Scheel¹ and Kip S. Thorne¹

¹*Theoretical Astrophysics 350-17, California Institute of Technology, Pasadena, CA 91125, USA*
(Dated: January 9, 2014)

We review discoveries in the nonlinear dynamics of curved spacetime, largely made possible by numerical solutions of Einstein’s equations. We discuss critical phenomena and self-similarity in gravitational collapse, the behavior of spacetime curvature near singularities, the instability of black strings in 5 spacetime dimensions, and the collision of four-dimensional black holes. We also discuss the prospects for further discoveries in geometrodynamics via observation of gravitational waves.

I. INTRODUCTION

In the 1950s and 60s, John Archibald Wheeler [1] speculated that curved, empty spacetime could exhibit rich, nonlinear dynamics — which he called *geometrodynamics* — analogous to the writhing surface of the ocean in a storm. Wheeler exhorted his students and colleagues to explore geometrodynamics by solving Einstein’s general relativistic field equations.

In 1965, Yakov Borisovich Zel’dovich, with his young protégés Andrei Doroshkevich and Igor Novikov [2], gave strong evidence that, when a highly deformed star collapses to form what would later be called a black hole, the hole’s curved spacetime, by its nonlinear dynamics, will somehow shake off all the deformations, thereby becoming a completely smooth, axially symmetric hole.

The Wheeler/Zel’dovich challenge of exploring geometrodynamics in general, and for black holes in particular, has largely resisted analytic techniques. In the 1980s and 90s, that resistance motivated the authors and our colleagues to formulate a two-pronged attack on geometrodynamics: *numerical solutions of Einstein’s equations* to discover general relativity’s predictions, and *observations of gravitational waves* from black-hole births and black-hole collisions to test those predictions. The numerical simulations have now reached fruition, and the observations will do so in the near future.

In this article—dedicated to the memory of Zel’dovich and Wheeler (who deeply respected each other despite cold-war barriers, and who were primary mentors for one of us, Kip Thorne)—we shall present an overview of some of the most interesting things we have learned about geometrodynamics from numerical simulations, and a preview of what gravitational-wave observations may bring. More specifically:

We shall describe geometrodynamical discoveries in four venues: *gravitational implosion*, where a phase transition, discrete self-similarity and critical behavior have been observed (Sec. II); the dynamics of spacetime near *singularities*, where richly chaotic behavior has been observed (Sec. III); the unstable evolution of a *black string* in five spacetime dimensions, where a dynamical sequence of strings linking black holes has been observed (Sec. IV); and *collisions of black holes* in four spacetime dimensions, where dynamical interactions of tidal tenses and frame-drag vortexes have been observed (Sec.

V). Then we shall briefly describe the prospects for observing some of these phenomena via *gravitational waves* (Sec. VI).

II. GRAVITATIONAL COLLAPSE: PHASE TRANSITION AND CRITICAL BEHAVIOR

The first numerical simulations to exhibit rich geometrodynamics were in 1993, by Matthew Choptuik [3], who was then a postdoc at the University of Texas. Choptuik simulated the spherical implosion (Fig. 1) of a linear, massless scalar field (satisfying $\square\Psi = 0$). The field’s energy, momentum and stress (which are quadratic in the field) generated spacetime curvature, with which the field interacted via the curvature’s influence on its wave operator \square . That interaction produced surprising nonlinear dynamics:

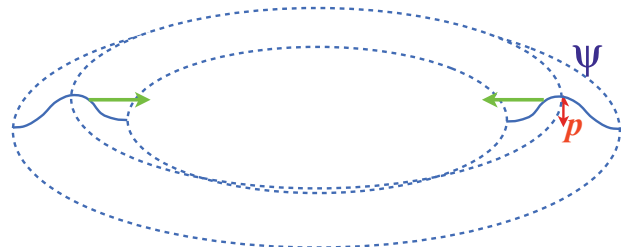


FIG. 1: The implosion of a scalar wave Ψ with amplitude p and a particular waveform.

If the wave amplitude p , for some chosen ingoing waveform, was larger than some critical value p_* , the implosion produced a black hole. If p was smaller than p_* , the imploding waves passed through themselves, travelled back outward, and dispersed. For $p = p_*$, the imploding waves interacted with themselves nonlinearly (via their spacetime curvature), producing a sequence of frequency doublings and wavelength halvings, with an intriguing, discretely self-similar pattern that was independent of the initial, ingoing waveform. Waves with ever decreasing wavelength emerged from the “nonlinearly boiling” field, carrying away its energy, and ultimately leaving behind what appeared to be an infinitesimal naked singularity (a region with infinite spacetime curvature, not hidden by

a black-hole horizon). One year after Choptuik’s simulations, the mathematician Demetrios Christodoulou [4] developed a rigorous proof that the endpoint, for $p = p_*$, was, indeed, a naked singularity.

The transition of the implosion’s endpoint, from black hole for $p > p_*$, to naked singularity for $p = p_*$, to wave dispersal for $p < p_*$, was a phase transition analogous to those that occur in condensed-matter physics. And, as in condensed matter, so also here, the phase transition exhibited scaling: For p slightly larger than p_* , the mass of the final black hole scaled as $M_{\text{BH}} \propto (p - p_*)^\beta$. For p slightly below p_* , the radius of curvature of spacetime at the center of the “boiling region” reached a minimum value, before field dispersal, that scaled as $\mathcal{R}_{\text{min}} \equiv (R^{\mu\nu\sigma\rho} R_{\mu\nu\sigma\rho})_{\text{max}}^{-1/4} \propto (p_* - p)^\beta$, with the same numerically measured exponent $\beta = 0.374$. Here $R_{\mu\nu\sigma\rho}$ is the Riemann curvature tensor.

Choptuik’s discovery triggered many follow-on simulations. Most interesting to us was one by Andrew Abrahams and Charles Evans [5], later repeated with higher resolution by Evgeny Sorkin [6]. In their simulations, the imploding, spherically symmetric scalar field was replaced by an imploding, axially symmetric (quadrupolar) gravitational wave — so they were dealing with pure, vacuum spacetime as envisioned by Wheeler. Once again, there was a critical wave amplitude p_* ; and for p near p_* the behavior was similar to the scalar-wave case, to within numerical error: for $p = p_*$, strong evidence for discretely self-similar evolution leading to an infinitesimal final singularity; for $p > p_*$, the same black-hole mass scaling $M_{\text{BH}} \propto (p - p_*)^\beta$; for $p < p_*$, the same spacetime-curvature scaling $\mathcal{R} \propto (p_* - p)^\beta$; and to within numerical accuracy, the scaling exponent was the same: $\beta = 0.38$ for the quadrupolar gravitational waves, and $\beta = 0.374$ for the spherical scalar wave. This is reminiscent, of course, of the universality one encounters in condensed-matter phase transitions.

For a detailed review of these and many other studies of critical gravitational implosion, see an article by Carsten Gundlach [7].

III. GENERIC SPACE-TIME SINGULARITIES

A. BKL Singularity

The singular endpoint of the implosions described above is *non-generic*, in the sense that no singularity occurs if p_* is only infinitesimally different from p .

However, there are other situations that lead to *generic* singularities.¹ This was demonstrated analytically in the

1960s by Roger Penrose, Stephen Hawking and others, using tools from differential topology [10]. In 1969–70, Vladimir Belinsky, Isaac Khalatnikov and Evgeny Lifshitz [11] used approximate differential-geometry techniques to deduce the geometrodynamical behavior of spacetime as it nears one generic type of singularity, a type now called *BKL*.

In the 1970s, 80s and 90s, there was much skepticism in the US and UK about this BKL analysis, because its rigor was much lower than that of the Penrose-Hawking singularity theorems. (This lower rigor was inevitable, because the geometrodynamical approach to a singularity is very complex—see below—and deducing its details is much more difficult than proving that a singularity occurs.) As a result, the BKL geometrodynamics came to be called, in the West, the *BKL conjecture*.

There was little hope for proving or disproving this “conjecture” by analytical techniques, so the skeptics turned to numerical simulations for probing it. After nearly a decade of code development, David Garfinkle in 2003 [12] carried out simulations which demonstrated that Belinsky, Khalatnikov and Lifshitz had been correct. The geometrodynamical evolution, approaching a BKL singularity, is as they predicted, though with one additional feature that they had missed: a set of nonlocal *spikes* in the spacetime curvature [13].

The BKL geometrodynamics can be described in terms of tidal-gravity observations by observers who fall into the BKL singularity on timelike geodesics; Fig. 2. As two observers, A and B, approach the singularity, they lose causal contact, in the sense that, after passing through A’s particle horizon (at point *P* in the diagram), B can no longer influence A. This causal decoupling is so strong, in the BKL spacetime, that spatial derivatives cease hav-

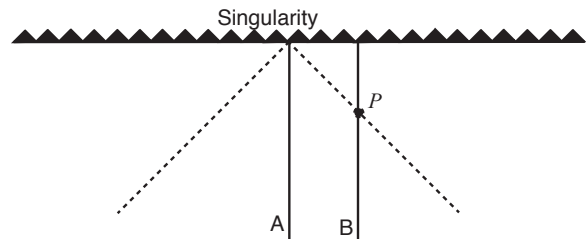


FIG. 2: The world lines of two observers, A and B, falling into a BKL singularity (the solid lines), and the *particle horizon* of observer A (dashed lines; a past light cone). Events outside the particle horizon can never influence observer A.

¹ Perhaps the most important generic singularity for astrophysics is one that arises when matter with negligible pressure is present. Leonid Petrovich Grishchuk in 1967 [8] showed that the matter, generically, undergoes gravitational collapse to form flat pan-

cakes with infinite density and curvature; and in 1970 Zel’dovich [9] showed that, astrophysically, pressure halts the collapse before the infinities but after the pancake structure has been strongly established. A few years later Zel’dovich realized that these pancakes, seen edge on, are filamentary structures that astronomers observe in the distribution of galaxies on the sky.

ing significant influence on the geometrodynamics, as the singularity is approached—there is a *spatial decoupling*—and as a result, it turns out, there is no correlation between the late-time observations of adjacent observers.

Each observer’s experience, when approaching the singularity, can be described in terms of the tidal gravitational field \mathcal{E}_{jk} that he feels. This tidal gravitational field has components, in the observer’s local Lorentz frame, that are equal to the space-time-space-time part of the Riemann curvature tensor.

$$\mathcal{E}_{jk} = R_{j0k0} . \quad (1)$$

The physical manifestation of the tidal field is a relative gravitational acceleration

$$\Delta a_j = -\mathcal{E}_{jk} \Delta x_j \quad (2)$$

of particles with vector separation Δx_j . (The tidal field acquires its name from the fact that the Sun’s and Moon’s tidal field produces the tides on the Earth’s oceans. In the Newtonian limit, the tidal field is $\mathcal{E}_{jk} = \partial^2 \Phi / \partial x_j \partial x_k$, where Φ is the Newtonian gravitational potential.)

Being a symmetric tensor, the tidal field can be described by three orthogonal principal axes (unit vectors $\mathbf{e}_1, \mathbf{e}_2, \mathbf{e}_3$), and their eigenvalues, $\mathcal{E}_{jj} \equiv \mathbf{e}_j \cdot \mathcal{E} \cdot \mathbf{e}_j$. If $\mathcal{E}_{11} < 0$, then an object is tidally stretched along its \mathbf{e}_1 principal axis, and similarly for the other principal axes. If $\mathcal{E}_{11} > 0$, the object is tidally squeezed along \mathbf{e}_1 . The tidal field, in vacuum, is trace-free, so its eigenvalues must sum to zero, which means there must be a squeeze along at least one principal axis and a stretch along at least one.

Figure 3 shows the pattern of stretches and squeezes experienced by an observer when falling into the BKL singularity. The pattern is divided, in time, into *cycles* and *eras*. During a single cycle, there is a stretch along one axis and a squeeze along the other two. Between cycles, the stretch axis switches to squeeze and the more strongly squeezing axis switches to stretch. At the end of each era, the axes rotate in some manner, relative to the observer’s local Lorentz frame, and the pattern begins over. The number of cycles in each era and the details of their dynamics are governed by a continued-fraction map that is chaotic, in the technical sense of chaos (extreme sensitivity to initial conditions). This chaos plays a key role in destroying correlations between the observations of adjacent observers as they approach the singularity.

The full details of this, as worked out by Belinsky, Khalatnikov and Lifshitz [11], occasionally are violated (numerical simulations reveal): A cycle gets skipped, and during that skip, there is an extreme spike in the tidal field that is more sensitive to spatial derivatives than expected, and whose details are not yet fully understood. See [13] and references therein.

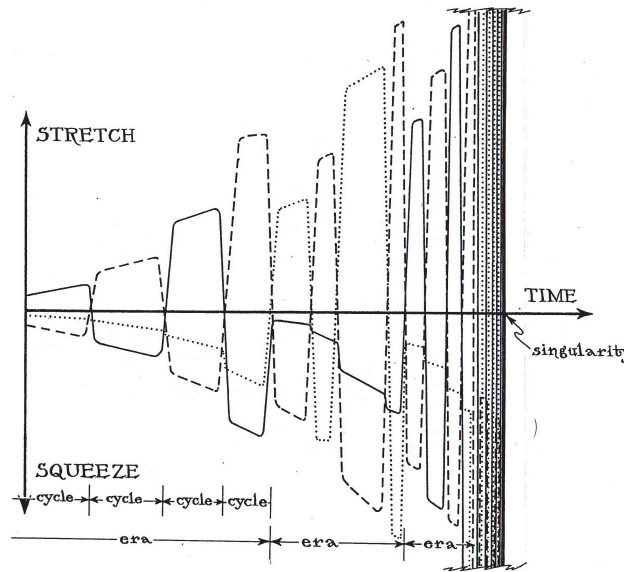


FIG. 3: The qualitative pattern of tidal stretches and squeezes experienced by an observer when falling into a BKL singularity. The three eigenvalues of the tidal field are plotted vertically as functions of time, with one axis shown solid, another dashed, and the third dotted. Adapted from [14]

B. Singularities Inside a Black Hole

This BKL behavior is speculated to occur in the core of a young black hole. However, numerical simulations are needed to confirm or refute this speculation.

As the black hole ages, the singularity in its core is speculated to break up into three singularities, one of BKL type, and two that are much more gentle than BKL. This speculation arises from the expectation that, just as the hole’s exterior spacetime geometry settles down into the quiescent, axially symmetric state described by the Kerr metric, so its interior will settle down into the Kerr-metric state, except near two special regions called *Cauchy horizons*, where the Kerr metric is dynamically unstable. Nonlinear geometrodynamics is thought to convert those Cauchy horizons into *null, generic singularities* (Fig. 4).

These singularities are null in the sense that ingoing or outgoing photons, in principle, could skim along them, not getting captured. The ingoing singularity (called a *mass inflation singularity*) is generated, according to approximate analytical analyses [16, 17], by radiation and material that fall into the black hole and pile up along the ingoing Cauchy horizon, there gravitating intensely. The outgoing singularity (called a *shock singularity* [15]) is generated by ingoing radiation that backscatters off the hole’s spacetime curvature, and then travels outward, piling up along the outgoing Cauchy horizon, there gravitating intensely. In both cases, the piling-up stuff could

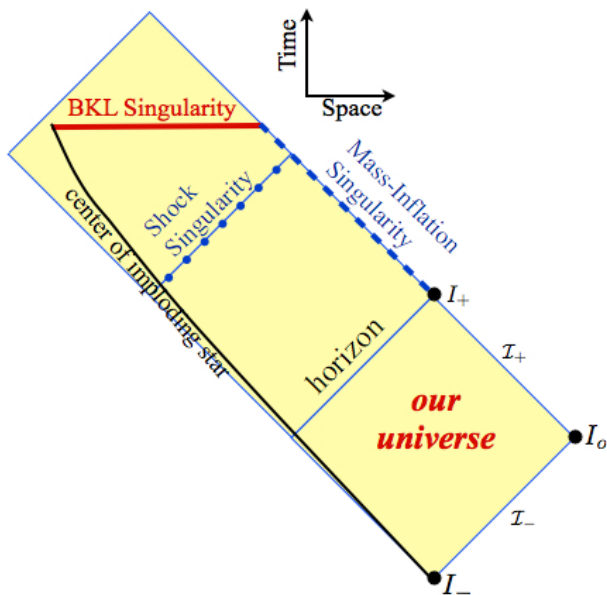


FIG. 4: Penrose diagram, depicting the causal structure outside and inside an old black hole, as best we understand it today. Ingoing and outgoing null rays (hypothetical photons) travel along 45 degree lines, and a conformal transformation has been used to compress our universe into a finite diamond in the diagram. The Kerr spacetime is shaded. The true spacetime is superposed on the Kerr spacetime; it is the region bounded by the center of the imploding star (thin left line), the BKL singularity (thick horizontal line), the mass-inflation singularity (dashed line), and the infinities of our universe: future timelike infinity labeled I_+ , future null infinity labeled \mathcal{I}_+ , spacelike infinity labeled I_0 , past null infinity labeled \mathcal{I}_- , and past timelike infinity labeled I_- . It might well be that the true spacetime ends at the shock singularity, and there is no BKL singularity beyond [15].

be gravitational waves rather than material or nongravitational radiation, in which case we are dealing with pure vacuum spacetime curvature—pure geometrodynamics.

Neither of these null singularities is oscillatory, but at both of them, the spacetime curvature goes to infinity (the radius of curvature of spacetime \mathcal{R} goes to zero). This divergence of curvature happens so quickly at the shock singularity, that objects *might* be able to pass through it, though with a destructive net compression along two dimensions and net stretch along the third. If so, they will likely then be destroyed in the BKL singularity.

The mass-inflation singularity is expected also to produce only a finite, not infinite, net compression and stretch of objects falling through. If anything survives, its subsequent fate is totally unknown.

These (highly informed) speculations, which arise from extensive, approximate analytically analyses, mostly perturbation theory, will be tested, in the coming few years, by numerical simulations. And just as the BKL conjecture missed an important phenomenon (the curvature

spikes), so these speculations about the geometrodynamics of black-hole interiors may fail in some modest, or even spectacular way.

For far greater detail on what we now know and speculate about the interiors of black holes and the bases for that knowledge and speculation, see [15] and references therein.

IV. BLACK STRING IN FIVE SPACETIME DIMENSIONS

A remarkable example of geometrodynamics has been discovered by Luis Lehner and Frans Pretorius [18], in numerical simulations carried out in five spacetime dimensions.

Lehner and Pretorius began with a *black string* in its equilibrium state. This black string is a vacuum solution of Einstein's equations in five spacetime dimensions, with metric

$$ds^2 = - \left(1 - \frac{2M}{r} \right) dt^2 + \frac{dr^2}{1 - 2M/r} + r^2(d\theta^2 + \sin^2\theta d\phi^2) + dz^2. \quad (3)$$

This is precisely a four-spacetime-dimensional Schwarzschild black hole, translated along the z axis in the fifth (spatial) dimension. The event horizon is at $r = 2M$; at fixed time t , it is a cylinder with spherical cross section, $R \times S^2$.

In 1993, Ruth Gregory and Raymond LaFlamme [19] proved, analytically, that such a black string is unstable. But little definitive was known about the instability's nonlinear, geometrodynamical evolution until Lehner and Pretorius's 2010 simulations [18]. They revealed that the string's horizon evolves as depicted in Fig. 5:

The string develops a sausage instability, analogous to that of a magnetically confined plasma in a Z -pinch, but with outgoing gravitational waves carrying off energy. This instability gives rise to a chain of five-spacetime-dimensional black holes linked by segments of shrunken black string—segments whose circumferences are far smaller than that of the original string. The instability then repeats on each shrunken string, producing smaller black holes linked by segments of more extremely shrunken string. Each successive sausage instability produces its smaller holes on an evolution timescale proportional to the string's circumference. These successively shorter timescales converge: An infinite sequence of instabilities, in finite time, presumably ends in a naked singularity.

Because these simulations assumed 2-sphere symmetry from the outset, we cannot be certain that their predictions are the black string's true geometrodynamical evolution. To learn the true evolution, we need simulations in five spacetime dimensions, that do not assume any symmetry. Such simulations are beyond current capabilities, but may be possible in a decade or so.

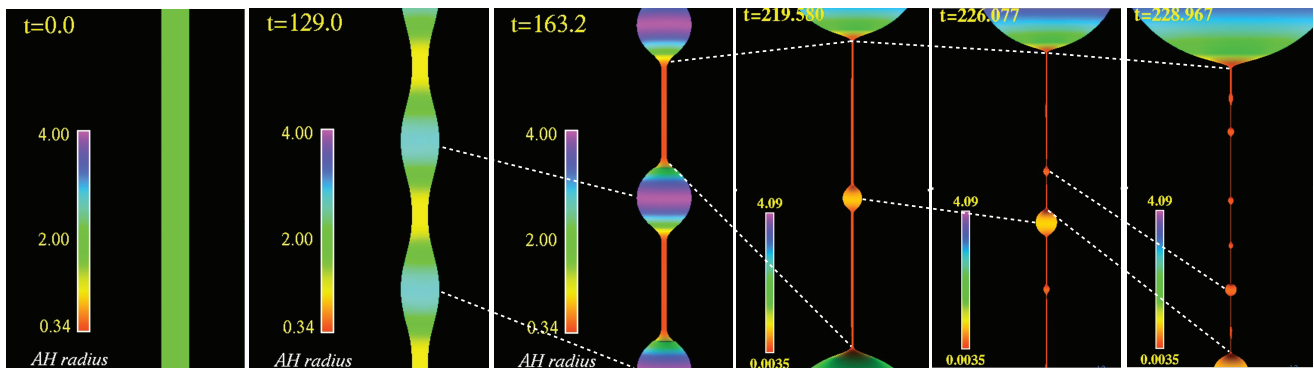


FIG. 5: A sequence of snapshots from a simulation of the geometrodynamical evolution of a black string in 5 spacetime dimensions, by Lehner and Pretorius [18]. Each snapshot is an embedding diagram of the black string’s event horizon: the horizon’s intrinsic geometry is the same as the intrinsic geometry of the depicted surface in flat space.

V. BLACK-HOLE COLLISIONS

Recent advances in numerical simulations have enabled the study of geometrodynamics in the violent collisions of two black holes—including the generation of gravitational waves, and the relaxation of the remnant to a single, quiescent, spinning black hole (as predicted by Zel’dovich, Doroshkevich and Novikov [2]). We and collaborators have developed a new set of so-called *vortex/tendex tools* for visualizing this black-hole geometrodynamics [20]. We will first describe these tools, and then we will use them to visualize the geometrodynamics of black-hole collisions.

A. Vortex-tendex tools

The gravitational field felt by a local observer is described by the Riemann curvature tensor $R_{\mu\nu\sigma\rho}$. Any such observer, freely falling or accelerated, can decompose Riemann into an “electric” part, \mathcal{E}_{jk} , defined by Eq. (1), and a “magnetic” part, \mathcal{B}_{jk} , defined by

$$\mathcal{B}_{jk} = \epsilon_{jpk} R_{pqk0}. \quad (4)$$

Here the indices are components on the observer’s local, orthonormal basis, the index 0 refers to the time component (*i.e.*, the component along the observer’s world line), Latin indices refer to the observer’s three spatial components, and ϵ_{jpk} is the spatial Levi-Civita tensor. Both \mathcal{E}_{jk} and \mathcal{B}_{jk} are symmetric and trace free in vacuum (the situation of interest to us).

As discussed in Section III A, \mathcal{E}_{jk} is called the *tidal field*, and describes the tidal stretching and squeezing experienced by objects in the observer’s local reference frame, according to Eq. (2). The “magnetic” quantity \mathcal{B}_{jk} is called the *frame-drag field*. The physical manifestation of this field is a relative precession, or dragging of inertial frames: two gyroscopes with vector separation Δx_j will precess relative to each other with angular

velocity

$$\Delta\Omega_j = \mathcal{B}_{jk}\Delta x_j. \quad (5)$$

This differential frame dragging is a general relativistic effect with no analogue in Newtonian gravity. Its global (non-differential) analog is one of the two relativistic effects recently measured by Gravity Probe B [21].

Note that the decomposition of the Riemann tensor into \mathcal{E}_{jk} and \mathcal{B}_{jk} depends on the observer’s reference frame. Different observers at the same location, moving relative to each other, will measure different tidal fields and frame-drag fields. This is the same situation as for classical electromagnetism, in which the electromagnetic tensor $F_{\mu\nu}$ can be decomposed into the familiar electric and magnetic field vectors, $E_j = F_{j0}$ and $B_j = \epsilon_{jpk} F_{pk}$, in the same observer-dependent manner. This correspondence between gravitation and electromagnetism motivates the use of the names “electric” and “magnetic” for \mathcal{E}_{jk} and \mathcal{B}_{jk} .

The frame-drag field \mathcal{B}_{jk} and the tidal field \mathcal{E}_{jk} are useful in describing geometrodynamics at the surface of a black hole (its event horizon). If \mathbf{n} is a unit vector normal to the hole’s horizon, with spatial components n^i , then we define the *horizon tendicity* $\mathcal{E}_{nn} \equiv n^j n^k \mathcal{E}_{jk}$ as the normal-normal component of the tidal field. For positive horizon tendicity, an object is tidally squeezed normal to the horizon, and for negative horizon tendicity, an object is tidally stretched normal to the horizon. This is illustrated in the left panel of Fig. 6. We call a region on the horizon with large tendicity a *horizon tendex*.

We can similarly define the *horizon vorticity* $\mathcal{B}_{nn} \equiv n^j n^k \mathcal{B}_{jk}$ as the normal-normal component of the frame-drag field at the surface of a black hole. For positive horizon vorticity, an object experiences a clockwise twist; for negative horizon vorticity, the twist is counterclockwise. We call a region on the horizon with large vorticity a *horizon vortex*. The horizon vorticity of a spinning black hole is illustrated in the right panel of Fig. 6.

We now turn to vortex/tendex tools in regions away from the horizon. In Section III A we discussed how,

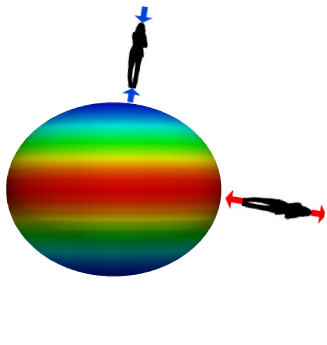


FIG. 6: A spinning black hole. **Left:** Colors represent horizon tendicity \mathcal{E}_{nn} . There is a positive (blue) tendex on each of the poles, and a negative (red) tendex on the equator. Green regions have small tendicity. **Right:** Colors represent horizon vorticity \mathcal{B}_{nn} . There is a negative (red) vortex on the north pole, and a positive (blue) vortex on the south pole. Green regions have small vorticity. The spin vector points out of the north pole.

at any point, \mathcal{E}_{jk} can be described by three orthogonal eigenvectors (unit vectors $\mathbf{e}_1, \mathbf{e}_2, \mathbf{e}_3$), and their eigenvalues, $\mathcal{E}_{\hat{j}\hat{j}} \equiv \mathbf{e}_{\hat{j}} \cdot \boldsymbol{\mathcal{E}} \cdot \mathbf{e}_{\hat{j}}$. We call the eigenvalue $\mathcal{E}_{\hat{j}\hat{j}}$ the *tendicity* associated with the corresponding eigenvector $\mathbf{e}_{\hat{j}}$; the tendicity measures the tidal stretching or squeezing of an object oriented along the eigenvector. In analogy with electric field lines, we define *tendex lines* as the integral curves along each of the three eigenvectors $\mathbf{e}_{\hat{j}}$. Whereas in electromagnetism there is a single electric field line passing through each point, in geometrodynamics there are generically three tendex lines passing through each point: one tendex line for each of the three eigenvectors of \mathcal{E}_{jk} . Because (in vacuum) \mathcal{E}_{jk} has vanishing trace, the eigenvalues must sum to zero, so generically there exist both positive and negative tendex lines at each point.

The left panel of Fig. 7 shows the tendex lines outside a rapidly rotating black hole. A collection of tendex lines with particularly large tendicity is called a *tendex*. The rotating hole has a fan-shaped, stretching (red) tendex sticking out of its equatorial horizon tendex, and a poloidal squeezing (blue) tendex that emerges from its north polar horizon tendex, and reaches around the hole to its south polar horizon tendex.

As with \mathcal{E}_{jk} , the frame-drag field \mathcal{B}_{jk} can be described by three orthogonal eigenvectors and their eigenvalues. An integral curve of one of these eigenvectors is called a *vortex line*, and the corresponding eigenvalue is the *vorticity* associated with that vortex line. The vorticity of a vortex line describes the twist, or differential frame dragging, experienced by an object oriented along that vortex line: positive vorticity corresponds to a clockwise twist, and negative vorticity corresponds to a counterclockwise twist.

The vortex lines associated with a spinning black hole are shown in the right panel of Fig. 7. A counterclockwise (red) *vortex* (collection of large-negative-vorticity lines) emerges from the horizon's north polar vortex, reaches

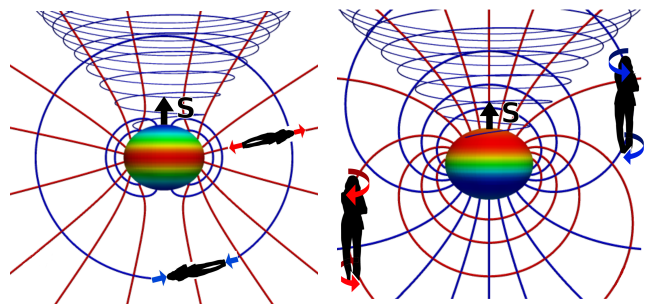


FIG. 7: Tendex lines (left panel) and vortex lines (right panel) near a spinning black hole. Lines with positive eigenvalues (tidal squeeze or clockwise twist) are shown blue, and lines with negative eigenvalues (tidal squeeze or counterclockwise twist) are shown red. At each point in space there are three intersecting tendex lines and three intersecting vortex lines.

around the south polar region and descends back into the horizon's north polar vortex. Similarly, a clockwise (blue) vortex emerges from the south polar horizon vortex, reaches around the north polar region and descends back into the south horizon vortex.

The black holes of Figs. 6 and 7 have stationary (time-independent) vortex and tendex structures. Vortex and tendex lines, and their associated vortices and tendexes, can also behave dynamically. The equations of motion for \mathcal{E}_{jk} and \mathcal{B}_{jk} are similar to Maxwell's equations. Like Maxwell, they have wavelike solutions—gravitational waves—in which energy is fed back and forth between \mathcal{E}_{jk} and \mathcal{B}_{jk} . Figure 8 shows vortex and tendex lines for a plane gravitational wave without any nearby sources. As the wave passes an observer, the tendicities and vorticities oscillate in sign with one oscillation per gravitational wave period, leading to an oscillatory stretch and squeeze in horizontal and vertical directions, and an oscillatory twist in diagonal directions, out of phase with the stretch and squeeze.

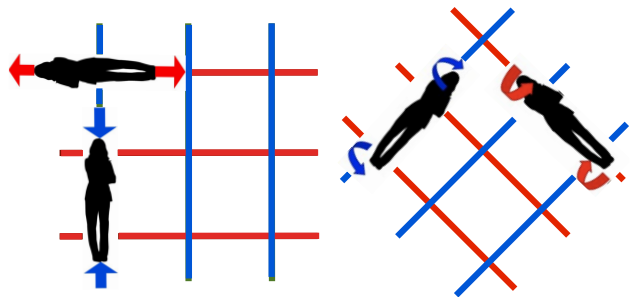


FIG. 8: Snapshot of vortex and tendex lines for a gravitational plane wave traveling into the page. Two orthogonal sets of tendex lines (left) are oriented 45 degrees with respect to two orthogonal sets of vortex lines (right). The third set of vortex (and tendex) lines is normal to the page, with zero vorticity (tendicity).

B. Black-hole collisions

We shall illustrate the geometrodynamical richness of black-hole collisions by describing the vortex/tendex behaviors in several numerical simulations. All these simulations were performed by members of the Collaboration to Simulate Extreme Spacetimes (SXS), which included numerical relativists from Caltech, Cornell, the Canadian Institute for Theoretical Astrophysics, and Washington State University at the time of these simulations, and has since been expanded. We are members of this collaboration, and one of us (Scheel) played a significant role in most of these simulations.

1. Head-on collision of two black holes with transverse spins

Our first example is a simulation [22] of the head-on collision of two transversely spinning black holes, depicted in Fig. 9.

As the black holes merge, the vortices retain their individuality. When the four vortices (one pair from each hole) discover each other, all attached to the same horizon, they begin to interact: each one tries to convert those adjacent to it into a replica of itself. As a result, they exchange vorticities; each oscillates back and forth between clockwise and counterclockwise. At the moment

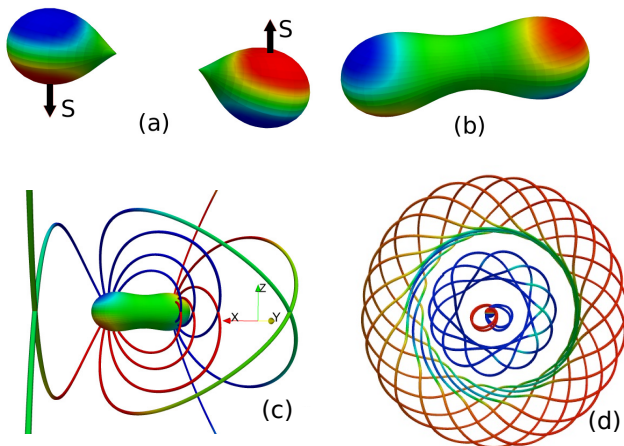


FIG. 9: The event horizons and vortex lines of spinning black holes, colliding head-on with transverse spins; from the simulation reported in [22]. (a) Horizon vortices and spin directions just before merger. (b) Horizon vortices just after merger, which retain their individuality. (c) Vortex lines linking horizon vortices of same polarity (red to red; blue to blue). Lines are color coded by vorticity (different scale from horizon). (d) Sloshing of near-zone vortices generates toroidal vortex loops (two shown here) composed of orthogonal vortex lines, traveling outward as gravitational waves; these are accompanied by intertwined tendex lines (not shown). The horizon, with attached vortex lines, is visible in the center. Figure adapted from [20].

when all are switching direction, so the horizon momentarily has zero vorticity, the vortex lines have popped off the horizon and joined onto each other, creating a toroidal structure, much like a smoke ring, that is beginning to travel outward. Simultaneously, adjacent to the horizon much of the oscillation energy is stored in tendexes, which then regenerate the horizon vortices, but with twist directions reversed. As the toroidal bundle of vortex lines travels outward, its motion generates toroidal tendex lines, intertwined with the vortex lines in just such a manner as to become, locally, the gravitational-wave structure described in Fig. 8 above.

The process repeats over and over, with successive, toroidal, tendex/vortex structures being ejected and morphing into gravitational waves. The waves carry away oscillation energy, and some oscillation energy goes down the hole, so the oscillations die out, with an exponential time of order an oscillation period.

2. Collision of identical, spinning black holes, in an inspiraling circular orbit

For collisions of orbiting (i.e. non head-on) black holes, the vortex and tendex lines similarly travel to the wave zone and become gravitational waves.

The left panel of Fig. 10 shows a schematic diagram of the horizon vortices and the vortex lines for the collision of two orbiting, spinning black holes that are about to merge. Just after merger, the horizon vortices retain their individuality, and travel around the horizon of the merged black hole, trailing their vortex lines outward and backward in a pattern like water from a spinning sprinkler head (shown schematically on the right of Fig. 10). In the wave zone, the vortex lines acquire tendex lines and become gravitational waves.

Similarly, the near-field tendex lines, attached to the merged hole's horizon tendexes, trail backward and outward in a spiral pattern, acquiring accompanying vortex lines as they travel, and becoming gravitational waves. These horizon-tendex-generated gravitational waves have the opposite parity from the horizon-vortex-generated waves; and there is a remarkable duality between the

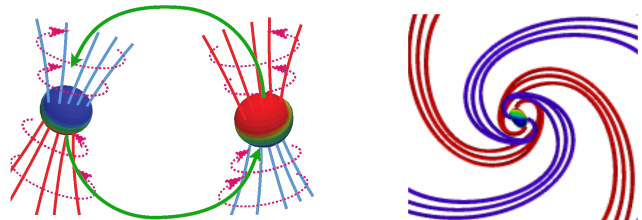


FIG. 10: **Left:** Schematic of vortex lines and horizon vortices for two orbiting, spinning black holes about to merge. **Right:** Schematic of vortex lines of the remnant black hole just after merger, showing vortex lines extending to large distances; the entire pattern is rotating counterclockwise.

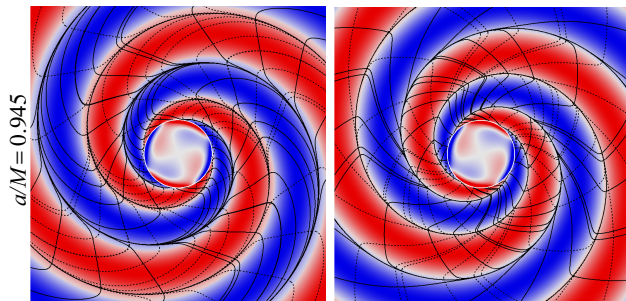


FIG. 11: Vortex and tendex structures for deviations from the final, Kerr black hole, at late times after the merger of a black-hole binary. These are the structures in the final hole’s equatorial plane, and the final hole has a dimensionless spin $S/M^2 = a/M = 0.945$. **Left:** Perturbations generated by horizon vortices—vortex lines (solid black for clockwise, dashed for counterclockwise), and vorticity of the dominant vortex at each point (colored blue for clockwise and red for counterclockwise). **Right:** Perturbations generated by horizon tendexes—tendex lines (solid black for squeeze, dashed for stretch), and tendicity of the dominant tendex (blue for squeeze and red for stretch). Adapted from Fig. 12 of [23].

two sets of waves [23]

Figure 10 is schematic. For a more precise depiction, we focus on the merged hole at late times, when it is weakly perturbed from its final, Kerr-metric state, and its perturbations are predominantly $\ell = 2$, $m = 2$ quasi-normal modes [23]. Then the perturbations of the frame-drag field, $\delta\mathcal{B}_{ij}$, generated by the horizon vortices, have the vortex lines and vorticities shown in the left panel of Fig. 11; and the perturbations of the tendex field, $\delta\mathcal{E}_{ij}$, generated by the horizon tendexes, have the tendex lines and tendicities show in the right panel. Notice that the two figures are very nearly identical, aside from sign (interchange of red and blue). This is due to the (near) duality between the two sets of perturbations.

3. Extreme-kick black-hole collision

An interesting example of geometrodynamics, and of the interplay between vortices and tendexes, is the “extreme-kick” black-hole collision first simulated, not by our SXS collaboration, but by Campanelli et al. [24] and others [25, 26]. Our collaboration has repeated their simulations, in order to extract the vortex and tendex structures.

In these simulations, two identical black holes merge from an initially circular orbit, with oppositely directed spins lying in the orbital (x, y) plane. The name “extreme-kick” arises because gravitational waves generated during the merger carry linear momentum preferentially in either the $+z$ or $-z$ direction, resulting in a gravitational recoil of the remnant black hole with speeds as high as thousands of km/s. The magnitude and direction of the recoil depends on the angle between holes’

identical spin axes, and the holes separations, at the moment of merger. This angle can be fine-tuned (for instance, to produce maximum recoil in the $+z$ direction) by adjusting the initial conditions in the simulation.

To understand the mechanism of the recoil, consider the remnant black hole just after merger. The left panel of Fig. 12 shows the horizon tendicity and the tendex lines emerging from the remnant black hole at some particular time. The tendex structure is rotating counterclockwise around the hole’s horizon. The rotating tendex lines acquire accompanying vortex lines as they extend into the wave zone in a pattern like that shown in the right panel of Fig. 11, and there they become gravitational waves. During merger, the horizon vortices (right panel of Fig. 12) lock onto the same rotational angular velocity as the horizon tendexes, and generate gravitational waves in the same manner, with a pattern that looks like the left panel of Fig. 11.

In the wave zone, the gravitational waves produced by the rotating near-zone tendexes and those produced by the rotating near-zone vortices superpose coherently, and the resulting radiation pattern depends on the angle between the horizon tendex labeled “E” and the vortex labeled “B” in Fig. 12. For the case shown, this angle is 45 degrees, with $\mathbf{E} \times \mathbf{B}$ in the $-z$ direction (into the page). This is the same as the structure of a gravitational wave propagating in the $-z$ direction (Fig. 8). As a result, the gravitational waves produced by the vortices and those produced by the tendexes superpose constructively in the $-z$ direction and destructively in the $+z$ direction, resulting in a maximum gravitational-wave momentum flow in the $-z$ direction and a maximum remnant recoil in the $+z$ direction.

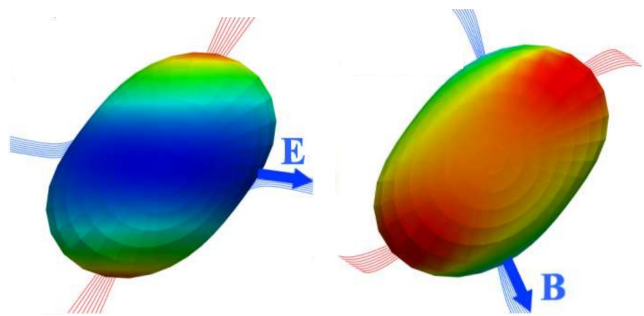


FIG. 12: Remnant horizon, shown in the xy plane, just after merger, for a superkick simulation tuned for maximum remnant recoil in the $+z$ direction; from a simulation presented in [20]. The black hole and vortex/tendex structures rotate counterclockwise. **Left:** Colors show horizon tendicity; tendex lines are shown emerging from the strongest horizon tendexes. **Right:** Colors show horizon vorticity; vortex lines are shown emerging from the strongest horizon vortices. Figure adapted from [20].

4. Generic black-hole collisions

The geometrodynamics behaviors of more general black hole collisions are now being explored numerically. For example, Fig. 13 shows trajectories of two black holes in a fully generic orbit. Vortexes from the larger, rapidly-spinning black hole pull the orbit of the smaller black hole into a complicated precession pattern. The spin directions of both black holes also precess as the holes orbit each other. Eventually a common apparent horizon² forms around the two individual apparent horizons, and the two holes merge into one. The Ricci scalar (approximately equal to -2 times the horizon tendicity) is shown on the two individual horizons and on the common horizon, at the moment the common horizon forms.

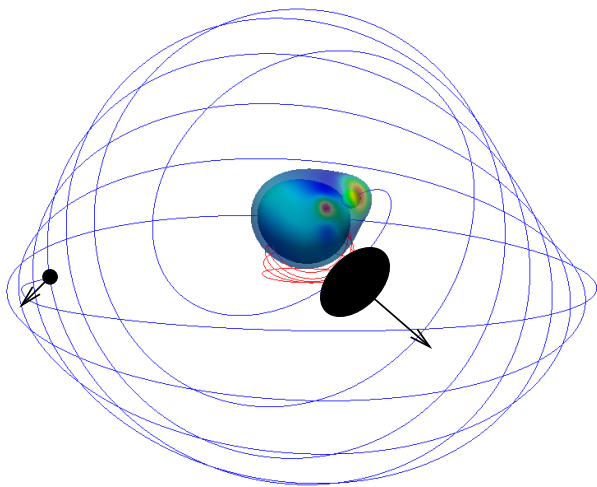


FIG. 13: The blue and red curves are the trajectories of the centers of two black holes in a generic orbit; from a simulation presented in [27]. The mass ratio of the two holes is 6:1, and the dimensionless spins of the larger and smaller holes are $S/M^2 = 0.91$ and 0.3 , respectively (compared to the maximum possible spin $S/M^2 = 1$). The initial black hole positions are shown in black, and the initial spins are shown as arrows. The spins are initially oriented in generic directions, so that the orbital plane precesses. Shown also are the apparent horizons of both holes, and the common apparent horizon that encloses them, at the time the common apparent horizon first forms. The horizons are colored by the scalar Ricci curvature, which is approximately -2 times the horizon tendicity.

² An apparent horizon is a surface of zero outgoing null expansion, and lies inside or on the event horizon. Apparent horizons are local quantities that are much easier to find in numerical simulations than are event horizons, because the location of the event horizon depends on the full future evolution of the spacetime.

5. Tidal disruption of a neutron star by a spinning black hole

Our final example illustrates the interaction of geometrodynamics and matter. Figure 14 shows a simulation of a neutron star orbiting a black hole, a binary system important for gravitational-wave detectors and possibly for high-energy astrophysical phenomena such as gamma-ray bursts. Here the black hole has 3 times the mass of the neutron star, and a dimensionless spin $S/M^2 = 0.5$ in a direction inclined approximately 45 degrees to the orbital angular momentum. When the orbit has shrunk sufficiently, because of energy lost to gravitational radiation, the black hole's tidal tendexes rip apart the neutron star, and its frame-drag vortexes then pull the stellar debris out of its original orbit and into the black hole's equatorial plane. If the black hole has a small enough spin or a large enough mass, the neutron star is not disrupted, but instead is swallowed whole by the black hole [28].

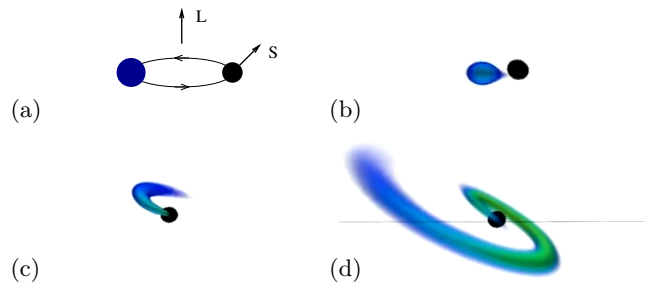


FIG. 14: Four successive snapshots of a collision between a black hole (black) and a neutron star (blue), viewed edge-on in the initial orbital plane; from a simulation reported in [29]. (a) The initial black-hole spin S is inclined with respect to the initial orbital angular momentum L . (b) The black hole's tendexes begin to rip apart the neutron star. (c) Some of the matter falls down the black hole, but some remains outside the horizon. (d) The black hole's vortexes pull the remaining matter into the black hole's equatorial plane, forming a disk and a tidal tail. Figure adapted from [29].

VI. GRAVITATIONAL-WAVE OBSERVATIONS

Geometrodynamics generically produces gravitational waves. We are entering an era in which these waves, generated by sources in the distant universe, will be detected on Earth.

A first generation of interferometric gravitational-wave detectors has operated at sensitivities where it would require luck to see waves. We were not lucky [30, 31].

Second generation detectors, much more advanced and complex in their design, are under construction. The first two of these (the advanced LIGO detectors in the U.S.) will begin operating in 2015 and should reach their design

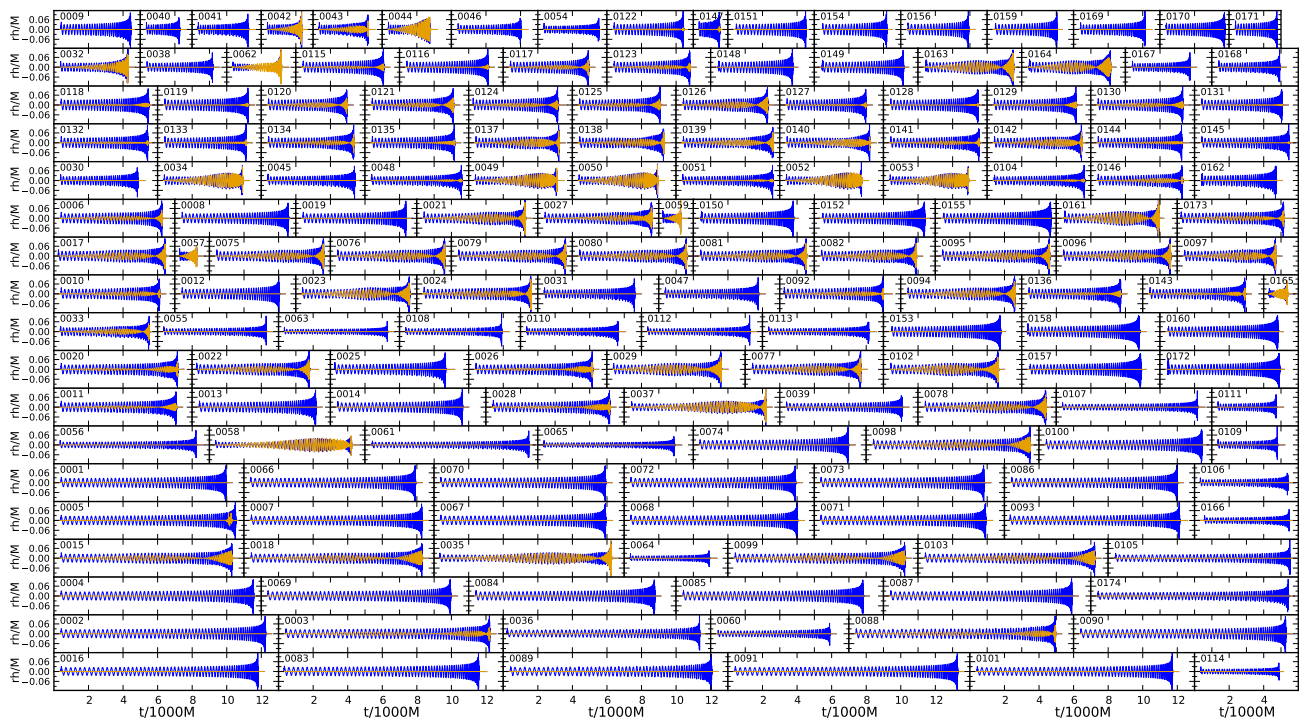


FIG. 15: A recent catalog of black-hole binary simulations from [27]. Shown are 174 waveforms, each with two polarizations (shown in blue and orange) in a sky direction parallel to the initial orbital plane. The unit on the time axis corresponds to 0.1 s for a binary with a total mass of 20 solar masses.

sensitivity by 2019, and perhaps sooner [32]. They will be joined a bit later by the advanced VIRGO detector in Europe, KAGRA in Japan, and an advanced LIGO detector in India [33]. These advanced detectors will cover a 1000 times larger volume of the universe than the initial detectors did, with estimated event rates for mergers of black-hole and neutron-star binaries ranging from a few per year to a few per week [34, 35, 36]. Plans are being developed for further improvements, which should increase the event rate by another factor ten or more, without major changes in detector design.

The most interesting gravitational-wave sources for these detectors, we think, are the dynamically evolving vortexes and tendexes attached to merging black holes, and to a black hole tearing apart a neutron star — the geometrodynamical phenomena discussed above.

The numerical relativity community is building a catalog of binary simulations and associated gravitational waveforms to underpin the advanced detectors' searches for these waves. Simulations of binary black holes with several hundred different sets of parameters (mass ratios and initial vectorial spins) have been completed [27, 37, 38, 39, 40, 41]; and many more are underway or planned. A sample of computed waveforms from our SXS collaboration is shown in Fig. 15.

Once waves are being detected, comparison of observed waveforms with those from simulations will be crucial for understanding the waves' sources. By such comparisons, can we deduce the sources' geometrodynamics and test

general relativity's predictions.

VII. CONCLUSIONS

Physicists have barely scratched the surface of geometrodynamics. As numerical simulations continue to improve and are used to explore more complicated and generic situations, we expect to learn more about the geometrodynamics of critical behavior, singularities, dynamical black holes, and other phenomena. We look forward to observations of gravitational waves from strongly gravitating astrophysical sources, which will enable us to test the geometrodynamical predictions of Einstein's equations for the first time.

Acknowledgments

We are grateful to Thorne's dear friend, the late Leonid Petrovich Grishchuk, for urging us to write this review article, and for many stimulating discussions. We thank members of the SXS collaboration and of the Caltech/Cornell Vortex/Tendex research group for data used for figures in Sec V, and for the work that made much of that section possible. We gratefully acknowledge support from the Sherman Fairchild Foundation, the Brinson Foundation, and NSF grants PHY-106881 and AST-1333520.

-
- [1] J. A. Wheeler, *Geometrodynamics* (Academic Press, New York, 1962).
- [2] A. D. Doroshkevich, I. D. Novikov, and Y. B. Zel'dovich, *Zhurnal Eksperimentalnoi i Teoreticheskii Fiziki* **49**, 170 (1965).
- [3] M. W. Choptuik, *Phys. Rev. Lett.* **70**, 9 (1993).
- [4] D. Christodoulou, *Ann. Math* **149**, 607 (1994).
- [5] A. M. Abrahams and C. R. Evans, *Phys. Rev. Lett.* **70**, 2980 (1993).
- [6] E. Sorkin, *Class. Quantum Grav.* **28**, 025011 (2011).
- [7] C. Gundlach, *Living Rev. Rel.* **2** (1999), 4, URL <http://www.livingreviews.org/lrr-1999-4>.
- [8] L. P. Grishchuk, *Soviet Physics JETP* **26**, 974 (1967), English translation of *Zhur. Eksp. Teor. Fiz.* **53**, 1699 (1967).
- [9] Y. B. Zel'dovich, *Astronomy and Astrophysics* **5**, 84 (1970).
- [10] S. W. Hawking and R. Penrose, *Proc. Roy. Soc. Ser. A* **314**, 529 (1969).
- [11] V. Belinskii, I. M. Khalatnikov, and E. M. Lifshitz, *Uspekhi Fiz. Nauk* **102**, 463 (1970).
- [12] D. Garfinkle, *Phys. Rev. Lett.* **93**, 161101 (2004).
- [13] W. C. Lim, L. Andersson, D. Garfinkle, , and F. Pretorius, *Phys. Rev. D* **79**, 123526 (2009).
- [14] K. S. Thorne, *Black Holes and Time Warps: Einstein's Outrageous Legacy* (W. W. Norton & Company, New York, 1994).
- [15] D. Marolf and A. Ori, *Phys. Rev. D* **86**, 124026 (2012).
- [16] E. Poisson and W. Israel, *Phys. Rev. D* **41**, 1796 (1990).
- [17] A. Ori, *Phys. Rev. D* **61**, 024001 (2000).
- [18] L. Lehner and F. Pretorius, *Phys. Rev. Lett.* **105**, 101102 (2010).
- [19] R. Gregory and R. Laflamme, *Phys. Rev. Lett.* **70**, 2837 (1993).
- [20] R. Owen, J. Brink, Y. Chen, J. D. Kaplan, G. Lovelace, K. D. Matthews, D. A. Nichols, M. A. Scheel, F. Zhang, A. Zimmerman, et al., *Phys. Rev. Lett.* **106**, 151101 (2011).
- [21] C. W. F. Everitt, D. B. DeBra, B. W. Parkinson, J. P. Turneure, J. W. Conklin, M. I. Heifetz, G. M. Keiser, A. S. Silbergleit, T. Holmes, J. Kolodziejczak, et al., *Phys. Rev. Lett.* **106**, 221101 (2011), URL <http://link.aps.org/doi/10.1103/PhysRevLett.106.221101>.
- [22] G. Lovelace, Y. Chen, M. Cohen, J. D. Kaplan, D. Koppel, K. D. Matthews, D. A. Nichols, M. A. Scheel, and U. Sperhake, *Phys. Rev. D* **82**, 064031 (2010), arXiv:0907.0869.
- [23] D. A. Nichols, A. Zimmerman, Y. Chen, G. Lovelace, K. D. Matthews, et al. (2012), 1208.3038.
- [24] M. Campanelli, C. O. Lousto, Y. Zlochower, and D. Merritt, *Phys. Rev. Lett.* **98**, 231102 (2007), gr-qc/0702133.
- [25] J. A. Gonzalez, M. D. Hannam, U. Sperhake, B. Brüggmann, and S. Husa, *Phys. Rev. Lett.* **98**, 231101 (2007), gr-qc/0702052.
- [26] C. O. Lousto and Y. Zlochower, *Phys. Rev. D* **83**, 024003 (2011), arXiv:1011.0593.
- [27] A. H. Mroue, M. A. Scheel, B. Szilagyi, H. P. Pfeiffer, M. Boyle, D. A. Hemberger, L. E. Kidder, G. Lovelace, S. Ossokine, N. W. Taylor, et al., *Phys. Rev. Lett.* **111**, 241104 (2013), arXiv:1304.6077, 1304.6077.
- [28] F. Foucart, *Phys. Rev. D* **86**, 124007 (2012), 1207.6304.
- [29] F. Foucart, M. D. Duez, L. E. Kidder, and S. A. Teukolsky, *Phys. Rev.* **D83**, 024005 (2011), arXiv:1007.4203 [astro-ph.HE].
- [30] J. Abadie et al. (LIGO Collaboration, Virgo Collaboration), *Phys. Rev. D* **85**, 082002 (2012), 1111.7314.
- [31] J. Aasi et al. (LIGO Scientific Collaboration, Virgo Collaboration), *Phys.Rev.* **D87**, 022002 (2013), 1209.6533.
- [32] J. Aasi et al. (LIGO Scientific Collaboration, Virgo Collaboration) (2013), 1304.0670.
- [33] S. Fairhurst, Proceedings of the ICGCC2011 conference, arXiv:1205.6611 (2012), 1205.6611.
- [34] A. T. Deller, M. Bailes, and S. J. Tingay, *Science* **323**, 1327 (2009), 0902.0996.
- [35] R. O'Shaughnessy, C. Kim, V. Kalogera, and K. Belczynski, *Astrophys. J.* **672**, 479 (2008), arXiv:astro-ph/0610076.
- [36] J. Abadie et al. (LIGO Scientific), *Class. Quant. Grav.* **27**, 173001 (2010), 1003.2480.
- [37] L. Pekowsky, R. O'Shaughnessy, J. Healy, and D. Shoemaker, *Phys. Rev. D* **88**, 024040 (2013), 1304.3176.
- [38] P. Ajith, M. Boyle, D. A. Brown, B. Brugmann, L. T. Buchman, et al., *Class. Quantum Grav.* **29**, 124001 (2012), URL <http://stacks.iop.org/0264-9381/29/i=12/a=124001>.
- [39] P. Ajith, M. Boyle, D. A. Brown, B. Brugmann, L. T. Buchman, et al., *Class. Quantum Grav.* **30**, 199401 (2013), URL <http://stacks.iop.org/0264-9381/29/i=12/a=124001>.
- [40] J. Aasi et al. (LIGO Scientific Collaboration, Virgo Collaboration, NINJA-2 Collaboration) (2014), arXiv/1401.0939, 1401.0939.
- [41] I. Hinder et al. (The NRAR Collaboration, Perimeter Institute for Theoretical Physics), *Class. Quantum Grav.* **31**, 025012 (2014), 1307.5307.